Quantum oscillations and topological properties of a YB_2 single crystal

Bishal Maity, Gourav Dwari, Suman Nandi, Vikas Saini, Vikash Sharma,
Bikash Patra, Ruta Kulkarni, Bahadur Singh,[*] and A. Thamizhavel[†]

Department of Condensed Matter Physics and Material Science, Tata Institute of Fundamental Research,
Homi Bhabha Road, Colaba, Mumbai 400005, India

The search for ideal quantum materials with symmetry-protected topological states continues to intrigue intense research activities in condensed matter physics. Here, we present single crystal growth, Fermi surface studies, and topological state analysis of a binary boride YB_2 that crystallizes in the hexagonal crystal structure with space group $P6/mmm$ and lattice constants $a = 3.304(2)$ Å, $c = 3.846(5)$ Å. The single crystal of YB_2 was grown by the Czochralski method, in a tetra-arc furnace. The anisotropic physical properties are reported by performing the electrical transport and magnetization measurements. The electrical resistivity confirms the metallic nature of YB_2 while the magnetization reveals that it is a diamagnetic material. Interestingly in the magnetoresistance and magnetization measurements, we observe quantum oscillations, namely, Shubnikov-de Haas (SdH) oscillations and de Haas van Alphen (dHvA) oscillations for the magnetic field direction parallel to [0001]. The quantum oscillations likely originates from a hole pocket centered at the A point. Our first-principles results unveil that YB_2 exhibits bulk nodal lines with interesting drumhead topological surface states.

I. INTRODUCTION

Topological semimetals, including Dirac, Weyl, and nodal line semimetals, are exotic conductors that have attracted tremendous recent research attention in condensed matter and materials physics owing to their disorder-resistant topological states and interesting physical properties. The topological semimetals are classified based on the symmetry and geometry of their electronic states [1–4]. Their unique electronic structure with relativistic quasiparticles gives rise to remarkable properties such as large unsaturated magnetoresistance [5], chiral anomaly [6], and anomalous Hall effect, among other phenomena. An extremely large magnetoresistance (XMR) in several of the binary compounds like WTe_2, $MoSi_2$, WSi_2, etc., have been reported recently [5,7–9]. Notably, the chirality of the charge transport and large anomalous Hall effect is being widely sought after for applications in next-generation low-power devices with inherent low background noise [10]. Although several pnictides and silicide-based binary compounds have been studied extensively for such topological transport features, the studies on binary borides are scanty. The boride compounds are interesting due to their high hardness and good electrical properties. MgB_2 is famously known to exhibit superconductivity with a transition temperature $T_c = 40$ K, close to the McMillan limit, and it is sensitive to substitution/doping [11]. Some of the boride compounds have a very good application potential; e.g. LaB_6 has emerged as the foremost choice for electron emitters for its low work function and high melting point [12]. There is some renewed interest in the binary boride systems where

electronic structure calculations and theoretical studies have been performed [13,14]. From the electronic structure studies, Zhang *et al.* [13] have identified that the metal diborides MB_2 (M = transition metal) fall into a new type of topological material possessing a pair of nodal rings coexisting with a pair of triply degenerate nodal points in the vicinity of the Fermi level. Given such interesting properties of binary diborides, here we investigate the anisotropic magnetotransport, Fermi surface, and electronic structure of YB_2. The boride compounds have a relatively high melting point and do not dissolve in many of the commonly used metallic fluxes at 1050 °C, which is the typical flux growth temperature for most of the intermetallic compounds. Specifically, an earlier study reported the single crystal growth of YB_2 from Y-rich melt at a very high temperature of 2000 °C [15]. Similarly, OsB_2 has been grown from a Cu-B melt at 1450 °C [16]. Hence, the growth of single crystals of diborides remains a challenge. In this work, we have successfully grown a single crystal of YB_2 using the Czochralski method in a tetra-arc furnace. The temperature dependence of resistivity confirmed that YB_2 is metallic and magnetization measurements revealed it to be diamagnetic as previously reported [17]. We also observed Shubnikov-de Haas (SdH) oscillations in magnetoresistance and de Haas-van Alphen (dHvA) oscillations in magnetization for magnetic field parallel to the [0001] direction. A detailed analysis of the magnetotransport and quantum oscillation properties has been performed along with the electronic structure calculations.

II. METHODS

The limited solubility of borides in metallic fluxes presents a formidable challenge in the synthesis of single crystals by flux growth at the commonly employed operating temperature

---

[*]Contact author: bahadur.singh@tifr.res.in
[†]Contact author: thamizh@tifr.res.in

of 1050 °C, typically used for the growth of intermetallic compounds. The binary phase diagram of Y and B depicts that YB_2 melts congruently at 2100 °C and hence it can be grown directly from its melt by the Czochralski method. We used stoichiometric quantities of Y and B with a purity of 99.9% (Alfa Aesar) and melted them in a tetra-arc furnace (Technosearch Corporation, Japan). The total amount of the starting material was about 10 g. The melting was done multiple times by flipping the ingot before each melt to ensure the homogeneity of the sample. A rectangular bar was cut from the resulting ingot and used as a polycrystalline seed for the crystal growth. The remaining polycrystalline ingot was remelted and the seed was carefully inserted into the melt and pulled rapidly at a rate of 100 mm/hr initially. Once the stable state was attained, we performed a necking process and continued the growth at the rate of 10 mm/hr for about six hours to obtain a cylindrical crystal of about 10 cm long. Energy dispersive analysis by x-ray (EDAX) was done to check the stoichiometry of the grown crystal. A small portion of the crystal was ground to a fine powder and x-ray diffraction (XRD) was performed at room temperature in a PANalytical x-ray diffractometer which uses a Cu-Kα ($\lambda = 1.5406$ Å) as the monochromatic source of x-rays. Laue diffraction in the back reflection geometry was performed to verify the single crystalline nature of the crystal and used to orient the crystal along its principal crystallographic directions. The single crystal of YB_2 was cut into rectangular bars in an electric discharge machine (EDM) using spark erosion. Electrical and magnetotransport properties were measured in the temperature range of 2–300 K in magnetic fields up to 14 T, using a physical properties measurement system (PPMS; Quantum Design, USA). Magnetization was measured using a vibrating sample magnetometer (VSM) attachment in PPMS which is equipped with a 14 T magnet.

The electronic structure calculations were carried out within the density functional theory [18] framework using the projector augmented wave (PAW) [19] method as implemented in the Vienna *ab initio* simulation package (VASP) [20,21]. The generalized gradient approximation with the Perdew, Burke, and Ernzerhof parametrization [22] was used to include the exchange-correlation effects. An energy cutoff of 480 eV was used for the plane-wave basis set and a $12 \times 12 \times 10$ Γ-centered k mesh was used for the bulk Brillouin zone sampling. The xcrysden program was used to visualize the Fermi surface [23]. A material-specific tight binding Hamiltonian was constructed using the atom-centered Wannier functions [24] with Y-d, B-s, and B-p orbitals. The surface states calculations were performed using the WANNIERTOOLS package [25]. The extremal areas and the corresponding quantum-oscillation frequencies were computed using the SKEAF code [26].

III. RESULTS AND DISCUSSION

A. X-ray diffraction

The room temperature powder XRD pattern is shown in Fig. 1(a). It unequivocally confirms the phase purity and crystal structure of the grown crystal. The crystal structure aligns with the space group $P6/mmm$ of the AlB$_2$-type structure
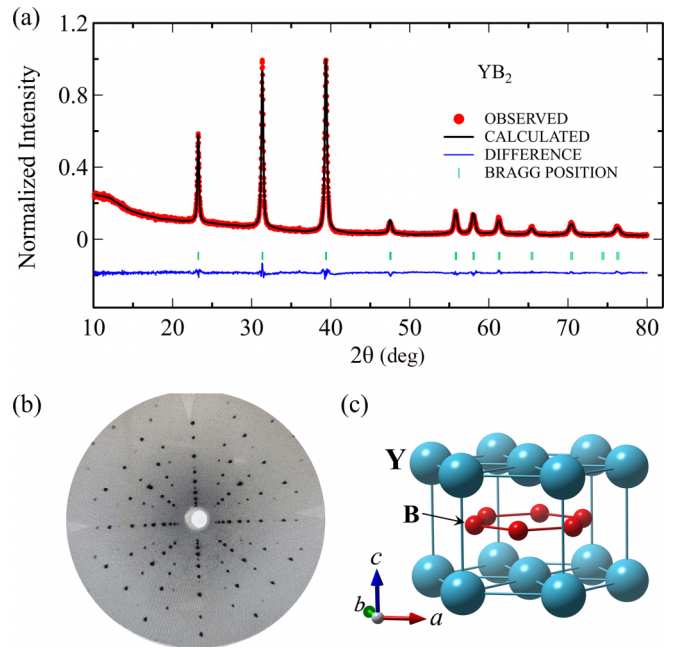

FIG. 1. (a) Room temperature powder XRD pattern of YB_2 with the Rietveld refinement shown by the black line. (b) Laue diffraction image in the back-scattered geometry of YB_2 depicting its (10$\bar{1}$0) plane. (c) Crystal structure of YB_2. The Y and B atomic layers are stacked along the hexagonal c axis.

as reported previously [17]. The lattice parameters extracted from the Rietveld refinement analysis [27] are $a = 3.304(2)$ Å and $c = 3.846(5)$ Å. The positional parameters of the Y and B atoms are (0, 0, 0) and (1/3, 2/3, 1/2), respectively, that occupy the standard Wycoff's positions 1a and 2d. We confirm the atomic composition of YB_2 using the EDAX analysis. Figure 1(b) presents the Laue diffraction pattern corresponding to (10$\bar{1}$0) of YB_2. The well defined and circular Laue spots attests good quality of the single crystal. In Fig. 1(c), we show the hexagonal crystal structure of YB_2, where the B layers are sandwiched between the Y atomic layers. Interestingly, the B atoms form a graphenelike honeycomb structure in the *ab* plane.

B. Electrical resistivity and magnetoresistance

The crystals were cut into small rectangular bars and electrical contacts were made for measuring resistivity in the transverse geometry for $I \parallel [10\bar{1}0]$, $B \parallel [0001]$ and $I \parallel [0001]$, $B \parallel [10\bar{1}0]$ directions. The temperature dependence of electrical resistivity, in the range of 2–300 K for current along the two principal crystallographic directions shows a metallic behavior [Figs. 2(a) and 2(b)]. There is only a subtle anisotropy in the electrical resistivity for the current along the two principal crystallographic directions. The resistivity decreases with temperature and becomes nearly temperature-independent for T less than 50 K. There are some previous reports on the successful growth of YB_2 using the floating zone method [28] and high temperature solution method using Yttrium as flux [15]. The residual resistivity of the crystal grown in Yttrium solution is 10 µΩ cm and the floating zone grown crystal has a resistivity of 39 µΩ cm at room tempera-
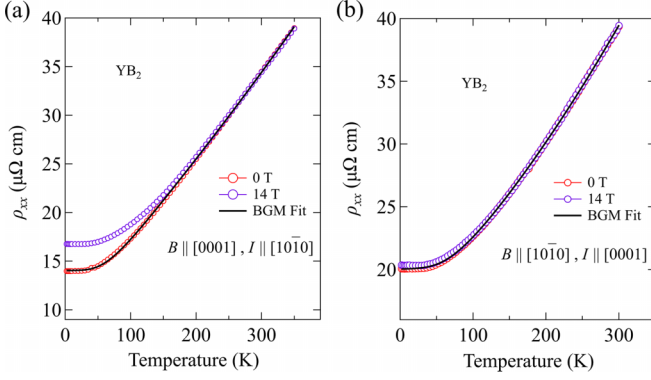
FIG. 2. Temperature dependence of resistivity at 0 and 14 T transverse magnetic fields. The BGM fit is shown by the black solid lines (see text for details).

ture. The measured residual resistivity of YB$_2$ is comparable with the flux grown crystal. This metallic behavior in resistivity is usually described using the Bloch-Grüneisen Mott (BGM) function [29], which is given as

$$\rho(T) = \rho_0 + A_{ee}T^2 + A_{ep}\left(\frac{T}{\Theta}\right)^5 \int_0^{\frac{\Theta}{T}} \frac{x^5}{(e^x - 1)(1 - e^{-x})}\, dx,$$

(1)

where the total resistivity is expressed as a sum of residual resistivity (ρ_0), resistivity due to electron-electron and electron-phonon interactions. A_{ee} represents the electron-electron scattering coefficient, A_{ep} denotes the electron-phonon scattering coefficient, and Θ is the Debye temperature. The fitting parameters for the resistivity data are listed below in Table I. The BGM fit suggests the electron-phonon interaction is significantly more than the electron-electron interaction in YB$_2$.

The electrical resistivity $\rho_{xx}(T)$ varies slightly at lower temperatures in an applied magnetic field of 14 T for current in the basal plane and the field along the c axis, while the variation is almost negligible for the field along the a axis [see Figs. 2(a) and 2(b)]. This is in stark contrast to other semimetallic systems where the electrical resistivity shows a huge upturn and plateau in magnetic fields [5,7,9,30], which is attributed to the electron-hole compensation. Figure 3(b) shows the MR ($\frac{\rho(B)-\rho(0)}{\rho(0)} \times 100\%$) for magnetic fields up to 14 T, measured at $T = 2$ K. The MR increases with the magnetic field and shows a saturation behavior at the highest magnetic field of 14 T as expected for an uncompensated system, which is confirmed by the Hall data. To obtain the charge carrier details, we have performed the Hall effect measurement in a five-probe geometry for the current along the [10$\bar{1}$0] and [0001] directions with a perpendicular
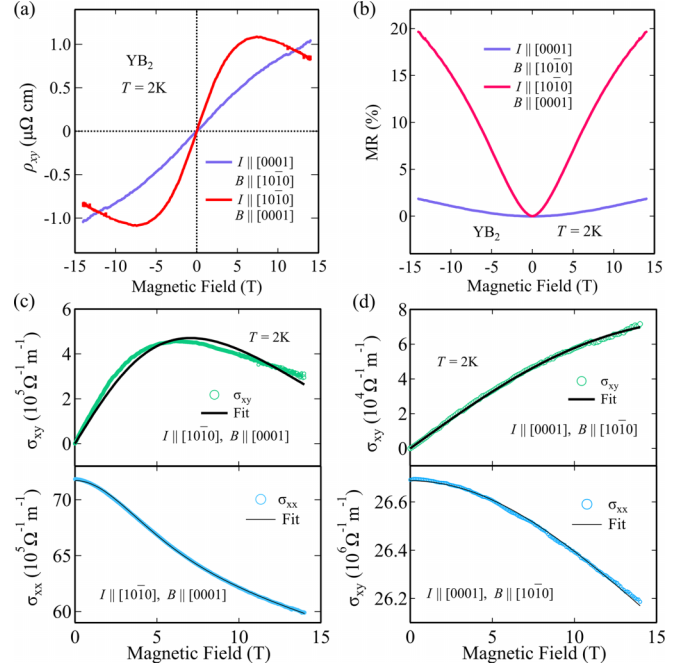

FIG. 3. Magnetic field dependence of (a) Hall resistivity and (b) transverse magnetoresistance for the two principal directions. (c), (d) Two band model fit for Hall conductivity for $B \parallel$ [0001] and [10$\bar{1}$0], respectively. The lower panels show the simultaneous fit to the magnetoconductivity.

magnetic field. We have avoided the contribution from ρ_{xx} in the Hall resistivity (ρ_{xy}) by performing an antisymmetrization $\rho_{xy}(B) = \frac{\rho_{xy}(B)-\rho_{xy}(-B)}{2}$. The Hall resistivity [Fig. 3(a)] is nonlinear and exhibits positive values for fields along both the principal crystallographic directions, suggesting holes are the majority carriers but the two-band model fitting shows a higher concentration of electrons. This is also reflected in our band structure calculations discussed below. Based on the analysis of the magnetotransport data on a two-band transport model, we have estimated the charge-carrier density and carrier mobility from the field dependence of transverse electrical resistivity (ρ_{xx}) and Hall resistivity (ρ_{xy}). According to the Drude model [31], the conductivity of individual carrier pockets (either electron or hole pockets) are summed up to get the total conductivity of the longitudinal and transverse counterpart of the conductivity tensor, given by

$$\sigma_{xx} = e\left[\frac{n_h\mu_h}{1 + (\mu_h B)^2} + \frac{n_e\mu_e}{1 + (\mu_e B)^2}\right],$$

(2)

$$\sigma_{xy} = e\left[\frac{n_h\mu_h^2}{1 + (\mu_h B)^2} - \frac{n_e\mu_e^2}{1 + (\mu_e B)^2}\right]B,$$

(3)

where n is the charge carrier density and μ represents the carrier transport mobility of the corresponding charge carriers (electron or holes represented by the suffixes e and h, respectively). The components of conductivity tensor can be deduced from the transverse magnetoresistivity (ρ_{xx}) and Hall resistivity (ρ_{xy}) data with the help of a tensorial inversion of the total resistivity matrix as $\sigma_{xx} = \rho_{xx}/(\rho_{xx}^2 + \rho_{xy}^2)$ and $\sigma_{xy} = \rho_{xy}/(\rho_{xx}^2 + \rho_{xy}^2)$ [32]. The calculated Hall conductivity and magnetoconductivity for $I \parallel$ [10$\bar{1}$0] and [0001] with

TABLE I. Parameters obtained from the BGM fit of the temperature dependence of the electrical resistivity measured at 0 T magnetic field [see Eq. (1) and Fig. 2].

	ρ_0 ($\mu\Omega$ cm)	Θ (K)	A_{ep} ($\mu\Omega$ cm)	A_{ee} $\mu\Omega$ cm K^{-2}
$I \parallel$ [0001]	20.05(1)	448(4)	75(2)	9.1(2) $\times$ 10^{-5}
$I \parallel$ [10$\bar{1}$0]	14.04(2)	400(5)	95(2)	4.5(1) $\times$ 10^{-5}

TABLE II. Fitting parameters for the electron and hole density and mobility obtained from the simultaneous fit of magnetoconductivity and Hall conductivity based on the two band model [Eqs. (2) and (3)].

	n_e (m^{-3}) $\times 10^{27}$	μ_e (m^2 V^{-1}s^{-1}) $\times 10^{-2}$	n_h (m^{-3}) $\times 10^{27}$	μ_h (m^2 V^{-1}s^{-1}) $\times 10^{-2}$
$I \parallel [0001]$ $B \parallel [10\bar{1}0]$	6.19(8)	0.22(3)	0.107(1)	2.57(2)
$I \parallel [10\bar{1}0]$ $B \parallel [0001]$	7.0(3)	0.49(1)	0.082(5)	10.5(4)

perpendicular magnetic fields are shown in Figs. 3(c) and 3(d), respectively. The solid lines are the best fit for the two-band model. The density of electrons and holes at the temperature of 2 K obtained from simultaneous fitting of the two-band model for Hall and magnetoconductivity are tabulated below in Table II. The different hole and electron concentrations imply that the charge carriers are not compensated. The magnitude of the charge carriers density further suggests that YB$_2$ is metallic with reasonably good mobility. It is evident from Table II that the hole mobility is dominant compared to the electron mobility.

C. Quantum oscillations studies

We have observed Shubnikov-de Haas (SdH) oscillations in the magnetotransport measurements of YB$_2$ for $I \parallel [10\bar{1}0]$, $B \parallel [0001]$ at high magnetic fields in the range of 10–14 T and for temperatures 2 K to as high as 10 K. The SdH oscillations are more prominent after background subtraction using a third-order polynomial as shown in Fig. 4.

The fast Fourier transform (FFT) of the background-subtracted data shows a unique frequency of 179 T [Fig. 5(a)]. Using the Onsager relation, $F = (\Phi_0/2\pi^2)A$, where Φ_0 is the magnetic flux quantum, we have estimated the extremal cross-sectional area (A) of the Fermi pocket equal to 1.71 nm^{-2}. The oscillations in background subtracted conductivity ($\Delta\sigma$) are well described by the Lifshitz-Kosevich (LK) equation. In the present case for small amplitude oscillations, we can directly
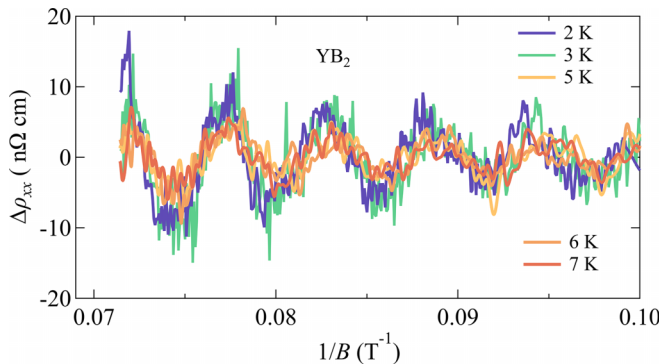
FIG. 4. Background subtracted SdH data for $I \parallel [10\bar{1}0]$ and $B \parallel [0001]$.
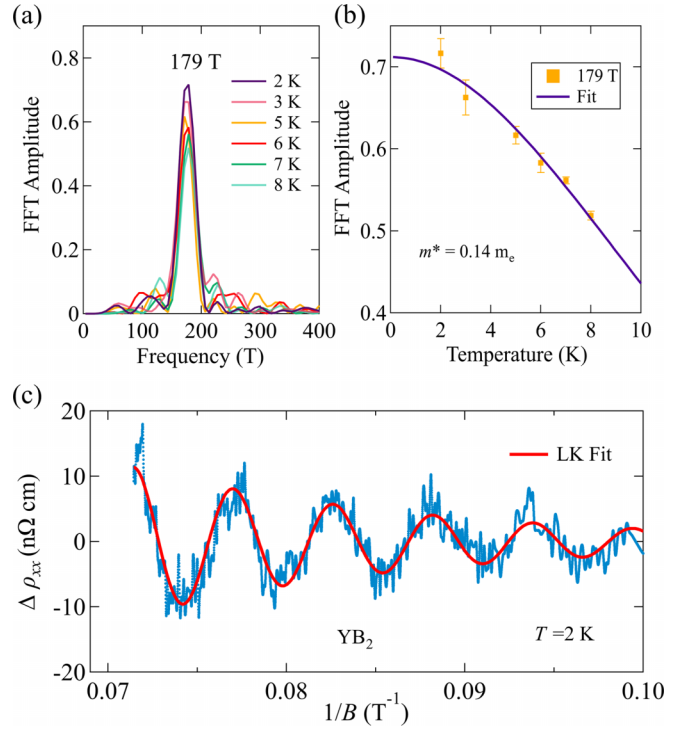
FIG. 5. (a) A frequency of 179 T is observed in SdH oscillations. (b) Mass plot of the obtained frequency. From the thermal damping factor, an effective mass of 0.14 m_e is obtained. (c) Lifshitz-Kosevich (LK) fit for the background subtracted resistivity at $T = 2$ K.

approximate to $\Delta\rho$, where [33,34]

$$\Delta\rho \propto \frac{\lambda T}{\sinh(\lambda T)} e^{-\lambda T_D} \cos\left[2\pi\left(\frac{F}{B} + \psi\right)\right]. \quad (4)$$

The amplitude of this frequency decreases with an increase in temperature, following the thermal damping factor $\frac{\lambda T}{\sinh(\lambda T)}$, where $\lambda \equiv (2\pi^2 m^* k_B)/(e\hbar B)$, m^* is the effective mass corresponding to the frequency F. From the temperature dependence of the frequency, we have estimated the effective mass as 0.143(6) m_e, which is shown in Fig. 5(b). The amplitude of the oscillations also decreases with a decrease in magnetic field which follows the relation $e^{-\lambda T_D}$, where T_D is the Dingle temperature and was extracted by fitting the data to LK equation for resistivity [Eq. (4)] which is shown in Fig. 5(c) and is estimated to be 9.7(2) K, for the 2 K oscillation data. From the Dingle temperature, we have estimated the single particle scattering rate $\tau = \hbar/2\pi k_B T_D$ as 1.252 × 10^{-13} s and quantum mobility ($\mu_q = e\tau/m^*$) as 1573 cm^2 V^{-1} s^{-1}. SdH oscillations were not observed for the direction $B \parallel [10\bar{1}0]$ and $I \parallel [0001]$ in our experimental setup at $T = 2$ K and 14 T magnetic field.

We have also observed de Haas-van Alphen (dHvA) quantum oscillations in the isothermal magnetization measurements in a VSM equipped with a 14 T magnet. YB$_2$ is a diamagnet as previously reported [17]. Figure 6 shows the observed oscillations measured at various fixed temperatures from 2 to 6.5 K, for the $B \parallel [0001]$ direction. We observe that the magnetization curves measured at different temperatures do not overlap on each other, which could be due
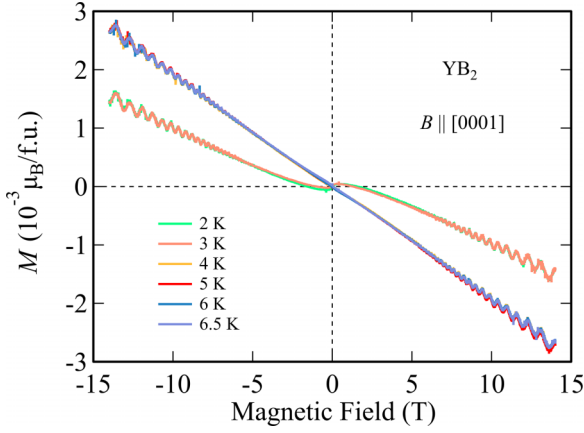
FIG. 6. dHvA oscillations in YB$_2$ at various temperatures for B || [0001].

to the difference in magnetization that occurs when measuring magnetization in zero field cooling (ZFC) and field cooling (FC) protocols. Since we did not follow these protocols during magnetization measurements with respect to magnetic field, we can expect such discrepancies. This however should not affect the oscillations amplitude. By subtracting the background contribution using a polynomial fit of the third order, we have extracted the oscillatory component and plotted it as a function of $1/B$ as shown in Fig. 7. From the FFT analysis, we observe a unique frequency of 205 T, this frequency and its temperature dependence are shown in Fig. 8(a). The estimated extremal area corresponding to this frequency is 1.96 nm^{-2}. We have estimated the effective mass of this frequency from its temperature dependence as 0.112(4) m_e and is shown in Fig. 8(b). The oscillatory part of the dHvA effect can be well explained by the Lifshitz-Kosevich expression, including the Berry phase, which is given as [33]

$$\Delta M \propto -B^{\frac{1}{2}} \frac{\lambda T}{\sinh(\lambda T)} e^{-\lambda T_D} \sin\left[2\pi\left(\frac{F}{B} + \psi\right)\right]. \quad (5)$$

Figure 8(c) depicts the fit to Eq. (5), and the estimated T_D from the fit is 10.4(8) K. We observe a difference in the SdH and dHvA frequency; this discrepancy is not fully understood at present and this warrants further investigation.
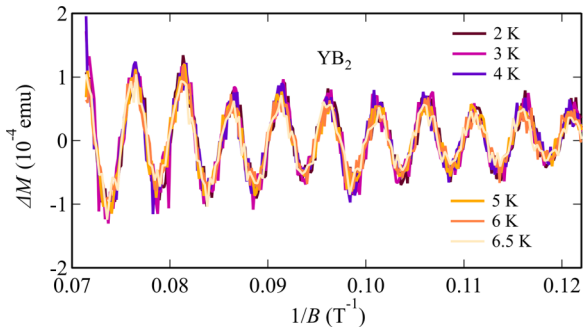

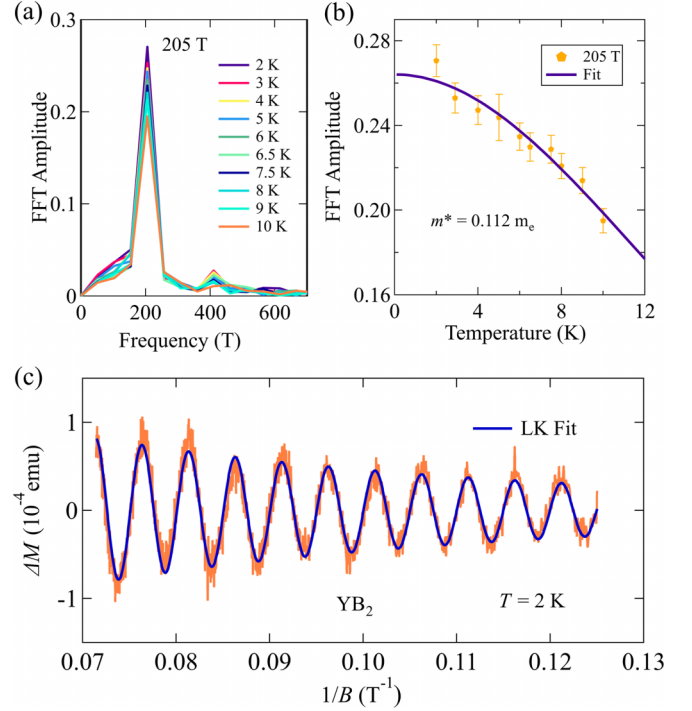FIG. 7. Background subtracted magnetization data of YB$_2$.

FIG. 8. (a) The FFT Amplitude as a function of frequency with a peak frequency of 205 T. (b) Fitting with the thermal damping factor, we get an effective mass of 0.112 m_e. (c) LK fit for the background subtracted magnetization data at $T = 2$ K.

D. Topological electronic structure and calculated quantum oscillations

The calculated band structure of YB$_2$ is shown in Fig. 9(a) along with the projected density of states (PDOS). It unveils a metallic state with both the electron and hole bands crossing the Fermi level in accord with our experimental results. The spin-orbit coupling (SOC) effects retain the essential features of band structure obtained without SOC. As evident from the PDOS, the low energy electronic states of YB$_2$ are dominated by Y-d and B-p orbitals. Figure 9(b) shows the calculated bulk Fermi surface that consists of two small hole pockets (blue and violet) centered around the A point and one large electron pocket (gray) consisting of two disconnected parts— one forming a closed loop around the Γ point and other lies near the zone boundary. The highly dispersive electron band touches the next conduction band, which forms a bulk Dirac cone at the K point, along the M-K and K-Γ directions [red dashed circle in Fig. 9(a)]. These band touchings form nodal rings around the K points at the $k_z = 0$ Å^{-1} mirror plane as shown in Fig. 9(c). Note that these band crossings lie away from the Fermi level and may have less influence on the transport properties of YB$_2$. To ensure the topological stability of these nodal rings, we calculate the Berry phase for an arbitrary circle enclosing the nodal line and estimate it to be π [35]. Figure 9(d) shows the calculated band structure of the (0001) surface. A drumhead surface state emanating from the projected nodal band crossings along the $\overline{M}$-$\overline{K}$ direction is evident. Interestingly, additional surface states cross with the drumhead surface states to form a surface Dirac cone at the $\overline{K}$ point. Note that this Dirac cone is distinct from the usual
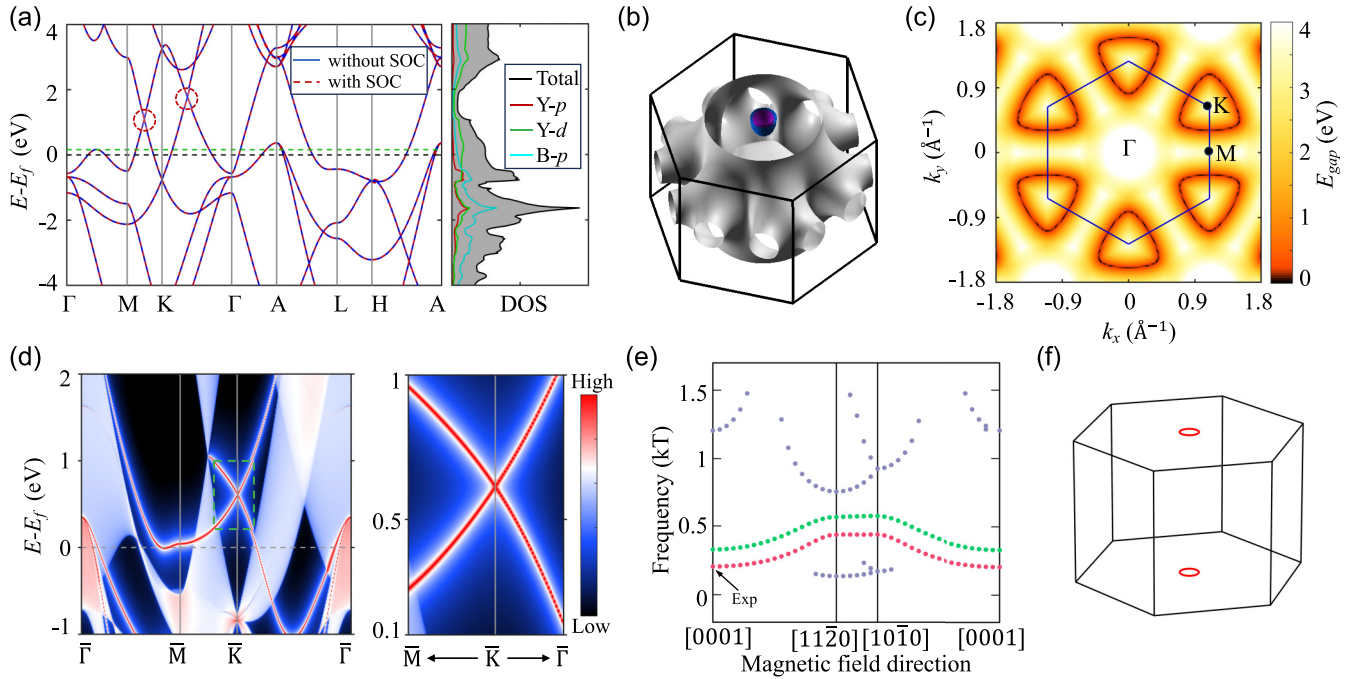
FIG. 9. (a) Bulk band structure (left) and density of states (right) of YB_2 without spin-orbit coupling. The red dashed circles highlight symmetry-protected nodal band crossings without SOC. The horizontal zero dashed line marks the Fermi level whereas the green dashed line denotes the shifted energy level ($E = E_f + 160$ meV) used to calculate quantum oscillations. (b) The associated Fermi surface with the coexisting electron (gray) and hole (blue and violet) pockets. (c) The planar distribution of the energy gap between two crossing bands in the $k_z = 0$ Å^{-1} plane. The color scale represents the band gap in eV. The gapless nodal lines are evident around the K point. (d) The (001) band structure of YB_2. The left panel shows a close up of the band structure highlighted in the dashed box. (e) Calculated angular dependence of dHvA frequency with magnetic field direction. The first point in the [0001] direction indicated by an arrow is the experimentally observed frequency and (f) the orbit giving the observed experimental frequency.

topological surface states seen in the nodal line semimetals. The surface Dirac bands preserve its linear dispersion over a large energy range and one of the bands crosses the Fermi level forming a saddle-point van Hove singularity at the $\overline{M}$ point. These features can be verified in various excitation based spectroscopic experiments. With the inclusion of SOC, there is a small opening of the gap ($\approx$25 meV) at the band crossing points. Regardless, the band structure retains the nodal lines and Fermi surface obtained without SOC.

The calculated angle dependence of quantum oscillations based on the bulk Fermi surface with the magnetic field direction are shown in Fig. 9(e). For B ∥ [0001], the frequency from the smaller hole pocket colored in violet centered at A [Fig. 9(b)] matches with the observed dHvA frequency of 205 T if the Fermi level is shifted by +160 meV. Such shifts in Fermi level are often necessary since the theoretical calculations assume ideal crystals, whereas the experimental samples contain defects, impurities, or self-doping effects [36]. This suggests that our crystal is electron-doped which is also reflected in the two-band model fitting of magnetoresistance and Hall resistivity data where the electron density is more than the hole density. The calculated frequency associated with the smaller hole pocket centered at the A point with change in the Fermi level and its effective mass (0.15 m_e) match reasonably well with our experimentally observed frequency and effective mass. The corresponding orbit of the Fermi pocket along the [0001] direction is plotted in red

color in the bulk Brillouin zone [Fig. 9(f)]. We also note that similar frequencies were observed for other hexaborides such as ScB_2 that share the same hexagonal crystal structure of YB_2 [37].

E. Summary

We have successfully grown a single crystal of YB_2 by the Czochralski method in a tetra-arc furnace, which is otherwise difficult to grow as a single crystal due to the dearth of suitable flux material. The phase purity and the crystal orientation were determined from the powder XRD and the Laue diffraction. The transport measurement revealed the metallic nature of YB_2 where resistivity decreases with a decrease in temperature and follows the BGM relation. The metallic state is consistent with our calculated bulk band structure and the Fermi surface. Moreover, the electrical resistivity showed a minimal response to the applied magnetic fields, with discernible SdH oscillations. The dHvA oscillations revealed a unique frequency of 205 T for the B ∥ [0001] direction which could be associated to the hole pocket centered at A. Further low temperature and high magnetic field angular dependence dHvA studies will be helpful for understanding the Fermi surface properties. Our theoretical analysis showed that YB_2 is a nodal line metal with unique topological drumhead surface states that form a surface Dirac cone centered at the $\overline{K}$ point of the (0001) surface Brillouin zone. Note that borides have been associated with high hardness and

are interesting in investigating various properties. Our study here revealed a reasonably good mobility, low effective mass, and topological surface states in YB$_2$. All these make YB$_2$ an appealing candidate for fundamental studies like excitation based spectroscopic studies and topological states-based applications.

[1] N. P. Armitage, E. J. Mele, and A. Vishwanath, Weyl and Dirac semimetals in three-dimensional solids, Rev. Mod. Phys. **90**, 015001 (2018).

[2] B. Q. Lv, T. Qian, and H. Ding, Experimental perspective on three-dimensional topological semimetals, Rev. Mod. Phys. **93**, 025002 (2021).

[3] M. Z. Hasan and C. L. Kane, *Colloquium:* Topological insulators, Rev. Mod. Phys. **82**, 3045 (2010).

[4] B. Singh, H. Lin, and A. Bansil, Topology and symmetry in quantum materials, Adv. Mater. Lett. **35**, 2201058 (2023).

[5] M. N. Ali, J. Xiong, S. Flynn, J. Tao, Q. D. Gibson, L. M. Schoop, T. Liang, N. Haldolaarachchige, M. Hirschberger, and N. P. Ong, Large, non-saturating magnetoresistance in WTe$_2$, Nature (London) **514**, 205 (2014).

[6] X. Huang, L. Zhao, Y. Long, P. Wang, D. Chen, Z. Yang, H. Liang, M. Xue, H. Weng, Z. Fang, X. Dai, and G. Chen, Observation of the chiral-anomaly-induced negative magnetoresistance in 3D Weyl semimetal TaAs, Phys. Rev. X **5**, 031023 (2015).

[7] M. Matin, R. Mondal, N. Barman, A. Thamizhavel, and S. K. Dhar, Extremely large magnetoresistance induced by Zeeman effect-driven electron-hole compensation and topological protection in MoSi$_2$, Phys. Rev. B **97**, 205130 (2018).

[8] S. Nakatsuji, N. Kiyohara, and T. Higo, Large anomalous Hall effect in a non-collinear antiferromagnet at room temperature, Nature (London) **527**, 212 (2015).

[9] R. Mondal, S. Sasmal, R. Kulkarni, A. Maurya, A. Nakamura, D. Aoki, H. Harima, and A. Thamizhavel, Extremely large magnetoresistance, anisotropic Hall effect, and Fermi surface topology in single-crystalline WSi$_2$, Phys. Rev. B **102**, 115158 (2020).

[10] M. J. Gilbert, Topological electronics, Commun. Phys. **4**, 70 (2021).

[11] C. Buzea and T. Yamashita, Review of the superconducting properties of MgB$_2$, Supercond. Sci. Technol. **14**, R115 (2001).

[12] H. Zhang, J. Tang, J. Yuan, Y. Yamauchi, T. T. Suzuki, N. Shinya, K. Nakajima, and L.-C. Qin, An ultrabright and monochromatic electron point source made of a LaB$_6$ nanowire, Nat. Nanotechnol. **11**, 273 (2016).

[13] X. Zhang, Z.-M. Yu, X.-L. Sheng, H. Y. Yang, and S. A. Yang, Coexistence of four-band nodal rings and triply degenerate nodal points in centrosymmetric metal diborides, Phys. Rev. B **95**, 235116 (2017).

[14] L.-P. Ding, Y. H. Tiandong, P. Shao, Y. Tang, Z.-L. Zhao, and H. Lu, Crystal structures, phase stabilities, electronic properties, and hardness of yttrium borides: New insight from first-principles calculations, J. Phys. Chem. Lett. **12**, 5423 (2021).

[15] Y. Song, X. Wu, B. Hu, and D. Ni, Growth of single crystals of YB$_2$ by a flux method, J. Cryst. Growth **223**, 111 (2001).

[16] Y. Singh, C. Martin, S. L. Bud'ko, A. Ellern, R. Prozorov, and D. C. Johnston, Multigap superconductivity and Shubnikov–de Haas oscillations in single crystals of the layered boride OsB$_2$, Phys. Rev. B **82**, 144532 (2010).

[17] V. V. Novikov, A. V. Matovnikov, T. A. Chukina, A. A. Sidorov, and E. A. Kul'chenkov, Heat capacity and lattice dynamics of yttrium diboride in the temperature range 5-300 K, Phys. Solid State **49**, 2034 (2007).

[18] P. Hohenberg and W. Kohn, Inhomogeneous electron gas, Phys. Rev. **136**, B864 (1964).

[19] P. E. Blöchl, Projector augmented-wave method, Phys. Rev. B **50**, 17953 (1994).

[20] G. Kresse and D. Joubert, From ultrasoft pseudopotentials to the projector augmented-wave method, Phys. Rev. B **59**, 1758 (1999).

[21] G. Kresse and J. Furthmüller, Efficient iterative schemes for *ab initio* total-energy calculations using a plane-wave basis set, Phys. Rev. B **54**, 11169 (1996).

[22] J. P. Perdew, K. Burke, and M. Ernzerhof, Generalized gradient approximation made simple, Phys. Rev. Lett. **77**, 3865 (1996).

[23] A. Kokalj, XCrySDen — a new program for displaying crystalline structures and electron densities, J. Mol. Model. **17**, 176 (1999).

[24] A. A. Mostofi, J. R. Yates, Y.-S. Lee, I. Souza, D. Vanderbilt, and N. Marzari, wannier90: A tool for obtaining maximally-localised Wannier functions, Comput. Phys. Commun. **178**, 685 (2008).

[25] Q. Wu, S. Zhang, H.-F. Song, M. Troyer, and A. A. Soluyanov, WannierTools: An open-source software package for novel topological materials, Comput. Phys. Commun. **224**, 405 (2018).

[26] P. Rourke and S. Julian, Numerical extraction of de Haas–van Alphen frequencies from calculated band energies, Comput. Phys. Commun. **183**, 324 (2012).

[27] H. M. Rietveld, A profile refinement method for nuclear and magnetic structures, J. Appl. Crystallogr. **2**, 65 (1969).

[28] R. W. Johnson and A. H. Daane, Electron requirements of bonds in metal borides, J. Chem. Phys. **38**, 425 (1963).

[29] N. Mott and H. Jones, *The Theory of the Properties of Metals and Alloys*, International Series of Monographs on Physics (Oxford University Press, Oxford, 1936).

[30] Y. Zhao, H. Liu, J. Yan, W. An, J. Liu, X. Zhang, H. Wang, Y. Liu, H. Jiang, Q. Li, Y. Wang, X.-Z. Li, D. Mandrus, X. C. Xie, M. Pan, and J. Wang, Anisotropic magnetotransport and exotic longitudinal linear magnetoresistance in WTe$_2$ crystals, Phys. Rev. B **92**, 041104(R) (2015).

[31] N. W. Ashcroft and N. D. Mermin, *Solid State Physics* (Saunders College, New York, 1976).

[32] C. M. Hurd, *The Hall Effect in Metals and Alloys* (Plenum Press, New York, 1972).

[33] D. Shoenberg, *Magnetic Oscillations in Metals* (Cambridge University Press, Cambridge, England, 1984).

[34] S. Sasmal, V. Saini, N. Bruyant, R. Mondal, R. Kulkarni, B. Singh, V. Tripathi, and A. Thamizhavel, Weak antilocalization and Shubnikov–de Haas oscillations in single crystal CaCuSb, Phys. Rev. B **104**, 205135 (2021).

[35] B. Patra, R. Verma, S.-M. Huang, and B. Singh, Role of effective mass anisotropy in realizing a hybrid nodal-line fermion state, Phys. Rev. B **108**, 235136 (2023).

[36] Y. Xia, D. Qian, D. Hsieh, L. Wray, A. Pal, H. Lin, A. Bansil, D. Grauer, Y. S. Hor, R. J. Cava, and M. Z. Hasan, Observation of a large-gap topological-insulator class with a single Dirac cone on the surface, Nat. Phys. **5**, 398 (2009).

[37] V. B. Pluzhnikov, I. V. Svechkarev, A. V. Dukhnenko, A. V. Levchenko, V. B. Filippov, and A. Chopnik, de Haas–van Alphen effect in the diborides ScB$_2$, ZrB$_2$, and HfB$_2$, Low Temp. Phys. **33**, 350 (2007).